JOURNAL OF GEOPHYSICAL RESEARCH, VOL. 100, NO. C3, PAGES 4943–4958, MARCH 15, 1995

Energetics of a naturally occurring shear instability

Harvey E. Seim[1] and Michael C. Gregg

Applied Physics Laboratory and School of Oceanography, College of Ocean and Fishery Sciences, University of Washington, Seattle

Abstract. Using observations of an energetic shear instability (Seim and Gregg, 1994), we examine the energy budget of the mixing event by comparing microstructure measurements of the dissipation rates of turbulent kinetic energy ϵ and turbulent potential energy χ_{pe} with changes in fine-scale velocity and density. Two sets of observations are used. The first set sampled the shear instability early in its evolution, when overturns occurred in strong stratification. The second set of observations found the same water vertically homogenized by turbulent mixing. In a frame of reference moving with the billows we solve a set of time-dependent energy equations to estimate the buoyancy flux J_b, turbulent production P, and strength of nonlocal forcing in the mean kinetic and mean potential energy budgets. The turbulent energy equations are approximately steady when evaluated for several buoyancy periods, simplifying to local balances. We find $J_b \approx \chi_{pe}/2 \approx -5.5 \times 10^{-7}$ W kg^{-1} and $P \approx \epsilon - J_b \approx 2.4 \times 10^{-6}$ W kg^{-1} to within a factor of 2. The decrease in mean kinetic energy is approximately locally balanced by P, but unlike the kinetic energy, only 25% of the increase in mean potential energy is explained by J_b. This implies no net radiation of energy into the surrounding stratified fluid, but the large uncertainties in J_b and P make this result tenuous. We find the flux Richardson, $R_f \equiv J_b/P \approx 0.22 \pm 0.1$; that is, one quarter of the turbulent energy released by the instability goes toward increasing the mean potential energy of the water column. The billows generated an average momentum flux of 0.22 Pa for more than an hour, and peak values exceeded 1.5 Pa. The average value is comparable to maximum momentum flux values in boundary layers over ice and under ice.

1. Introduction

This article continues the analysis of a high Reynolds number shear instability in a stratified flow. *Seim and Gregg* [1994], hereinafter referred to as part 1, is a detailed presentation of the observations; this paper examines the energetics in a control volume containing the instability event. We compare changes in the kinetic energy and potential energy to the dissipation rates of turbulent kinetic energy and turbulent potential energy within a control volume and estimate how much energy is radiated by the mixing event. The impact of the instability on the large-scale fields is quantified, and the efficiency of the resultant turbulent mixing is estimated. We also examine conditions at the onset of instability.

The formulation of an energy budget of the baroclinic flow for both the mean and turbulent components of the flow is new. Though equations describing the kinetic energy balance can be found in standard texts, e.g., *Monin and Yaglom* [1971], there are no similar formulations for the potential energy balance. This is apparently due to the difficulty of defining mean potential energy for an arbitrary fluid volume; in general, it can only be expressed in integral form. To avoid this problem, we decompose the potential energy into background and available components using a sorting algorithm originally proposed by *Thorpe* [1977]. A formalism for using sorting in three dimensions to decompose the potential energy has recently been advanced by *Winters et al.* [1995]. The sorting adiabatically redistributes all the fluid parcels in a volume into a one-dimensional monotonically increasing function. The sorting index z_* specifies the reference position of a fluid parcel in a state of minimum gravitational potential energy achievable with the collection of fluid parcels. This decomposition has the great advantage of isolating changes in potential energy due to diabatic processes: in a closed system the background (sorted) state only changes through a divergence of the diapycnal flux. This attribute makes the decomposition ideal for mixing-process studies.

We are unaware of any other microstructure studies that have obtained repeated observations of a specific mixing event. These data present an opportunity to test whether a local balance of production and dissipation, assumed in nearly all parameterization schemes [*Gregg*, 1987], is appropriate in a natural setting. They

[1]Now at Woods Hole Oceanographic Institution, Woods Hole, Massachusetts

Paper number 94JC03199.
0148-0227/95/94JC-03199$05.00

also provide an opportunity to examine whether shear instabilities in a stratified fluid radiate internal waves during their decay, as suggested by *Fritts* [1979, 1984]. Though this single event lacks the statistical significance of laboratory studies, we feel the uniqueness of the observations warrants a detailed analysis.

Because we cannot be certain of the exact form of evolution of the shear instability, which we call billows, we adopt a coordinate system moving with the billows to evaluate the energetics. In this coordinate system, changes in energy are correctly measured for billows growing in time, in space, or a mixture of both. The reference frame is Lagrangian because it minimizes the importance of advection, but errors in tracking the billows in the accelerating flow make our actual coordinate system quasi-Lagrangian. Further, by choosing vertical bounds of the control volume that support minimal vertical fluxes, we make the energy balance as local as possible.

We first describe how, when, and where the event was observed, explain the billows-following coordinate system, and outline the procedure used to pair profiles for comparison. The energy balance equations are then developed in section 3. The measured components of the energy balance are presented in section 4, along with an interpretation of their trends. We solve the balance equations to estimate buoyancy flux, turbulent production, and energy radiated/adsorbed by the event in section 5. The results and implications of the study are summarized in section 6.

2. Background

2.1. Instrumentation

Data used in this study were collected with a 153-kHz acoustic Doppler current profiler (ADCP) and with the advanced microstructure profiler (AMP). The ADCP continuously measures the vertical profile of horizontal currents, collecting profiles at approximately 2 Hz. Water velocities are measured along four acoustic beams (in a Janus configuration) which are then transformed into geographic coordinates, yielding estimates of east u, north v, and vertical w velocity. The sampling volume of the ADCP is determined by the beam separation. The horizontal separation is 35 m at 0.3 MPa (1 MPa $\approx$ 100 m) and increases to 75 m at 0.65 MPa. Averaging is required because the instantaneous measurements are quite noisy. Averaging over 2 min in time and over 4 m in the vertical reduces the rms error to ± 1.4 cm s^{-1}. With an average ship speed of 0.5 m s^{-1} relative to the billows, 2-min averages correspond to 60-m horizontal spatial averages, roughly the billow wavelength of 70 m. Owing to poor navigation and no bottom tracking, we lack absolute velocities and therefore estimate the barotropic current using a tidal model (part 1).

AMP is a loosely tethered, free-falling profiler which carries sensors to measure temperature, conductivity, pressure, microscale temperature, and horizontal velocity. Our standard processing produces temperature T, salinity S, and density ρ profiles with 0.1-m resolution, and profiles of the dissipation rates of turbulent kinetic energy ϵ and temperature variance χ with 0.5-m resolution. Details of how we form derived quantities from the AMP profiles are given in part 1.

2.2. Setting

In March 1988 we began a survey cruise of the Puget Sound, Washington, system, which was intended to identify where and when turbulent mixing was most intense. Our first samples were collected in Admiralty Inlet, the 30-km long, 70-m deep tidal channel that connects Puget Sound to the inner Strait of Juan de Fuca. On average, there is a strong exchange flow through Admiralty Inlet, fresh water from river runoff flowing seaward, and more saline water from the strait moving landward into the sound.

As ebb tide began on March 23, we were working off Bush Point near the midpoint of Admiralty Inlet. In the inlet, Bush Point forms a pronounced lateral constriction which acts as an internal hydraulic control during parts of the tidal cycle (part 1). While steaming with the current, we ran through a kilometer-long set of billows, centered at 0.5 MPa, just downstream (north) of Bush Point. After reversing course, we roughly held position and the current advected the same set of billows by us. This allowed us to collect two sets of measurements within an active set of billows separated in time by several buoyancy periods.

The formation of the billows is tied to the channel geometry (part 1). Using a high-frequency echo sounder, we imaged the initial development of the billows. They were found only downstream of Bush Point, and changes in the outer scales of the billows were consistent with a spatially growing disturbance initiated just downstream of the constriction. The flow was in transition from internally subcritical flow throughout to controlled flow (i.e., transcritical) as the billows formed, and the interface movement associated with the transition produced a longitudinal density structure within the set of billows. This longitudinal density structure made the formation of the billows time-dependent and precludes interpreting the event as a spatially steady process.

Persistent turbulent flow is characteristic of the area where the data were collected; the tidal channel is rugged and deep, with a 0.5 m s^{-1} baroclinic exchange flow and tidal currents exceeding 1 m s^{-1}. Combined, these flows generate many instabilities and result in an average ϵ of 5.9×10^{-7} W kg^{-1} between 0.1 and 0.9 MPa for 49 profiles collected near Bush Point during this tidal cycle. This is 500 times typical values of ϵ in the ocean thermocline.

2.3. Billows-Following Coordinate System

From the ADCP data we know the ship's velocity relative to 0.5 MPa, the pressure at which the bil-

lows were centered. All our observations fell within a 600 m × 2200 m rectangle moving downstream (south to north) at the average speed of the flow at 0.5 MPa. Figure 1 is a cartoon of the position of the box relative to the lateral constriction as a function of time, showing where microstructure profiles were collected within the box. Because billows have roughly zero phase velocity and are advected by the mean flow [*Ho and Huerre*, 1984], a coordinate system relative to 0.5 MPa follows the average motion of the billows. Repeated measurements at a given point in this coordinate system can be used to estimate the total derivative (where $D/Dt \approx \partial/\partial t + V\partial/\partial y$). The shading in Figure 1 shows when and where active billows are found within the box; AMP drops 5854–5866 sample active billows in the downstream (northern) half of the box. (Only the last two digits of the drop numbers are used in the figures and will be used subsequently.)

The alongstream density structure within the billows is apparent in a series of density profiles collected on the downstream and upsteam passes (Figure 2). The interface is higher at the south end of the set, causing density at a given depth to increase to the south. The longitudinal density structure is associated with the transition to hydraulically controlled flow at Bush Point, the upper layer thinning as it becomes supercritical. The profiles in Figure 2b, collected several kilometers downstream from those in Figure 2a, demonstrate that the density structure persists well downstream of the control.

The vertical bounds of the control volume (the box in Figure 1) are chosen to coincide with minimal turbulent activity to minimize the importance of turbulent fluxes across the surface of the control volume. The vertical extent of the billows is obvious in the average profiles of the root-mean-square displacement L_{rms} [*Thorpe*, 1977] and buoyancy scale $L_b \equiv (\epsilon/N^3)^{1/2}$ (Figure 3). The billows are about 20 m tall, extending from 0.4 to 0.6 MPa. Because Admiralty Inlet is al-

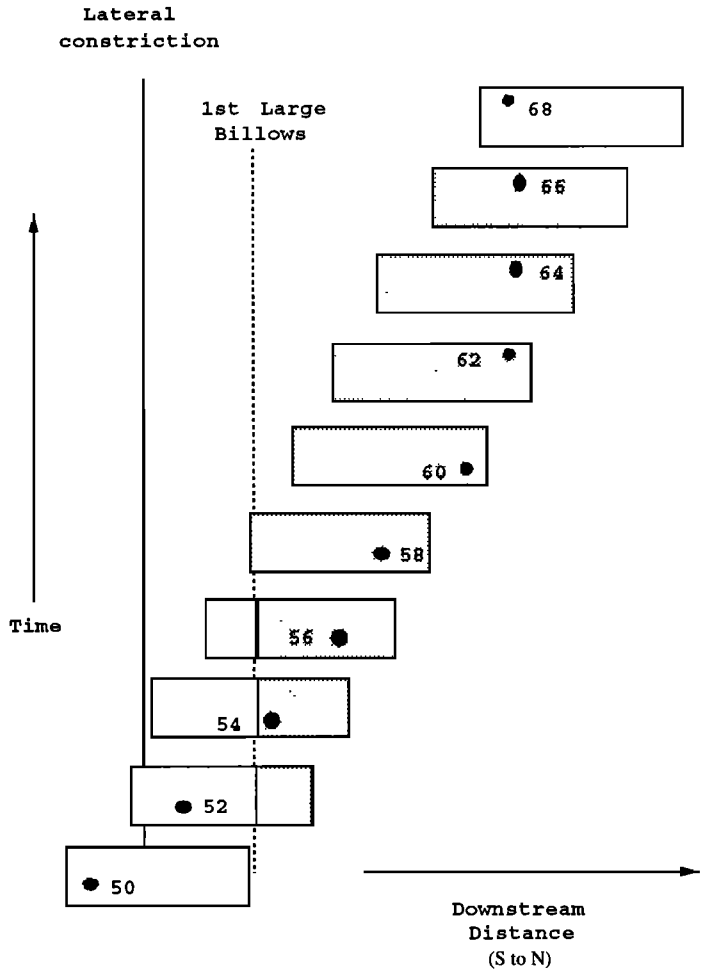

Figure 1. A distance-time diagram, showing the position of the sampling volume and specific profiles, relative to the lateral constriction. The control volume, which is 600 m by 2200 m, moves steadily downstream (north) along a diagonal in the diagram. The position of the box is shown approximately every 12 min. The point where billows form, slightly downstream of the constriction, is shown by shading within the sampling volume. Solid circles are the positions of advanced microstructure profiler (AMP) profiles within the control volume; only the last two digits of the profile numbers are used, i.e., 50 is AMP 5850.

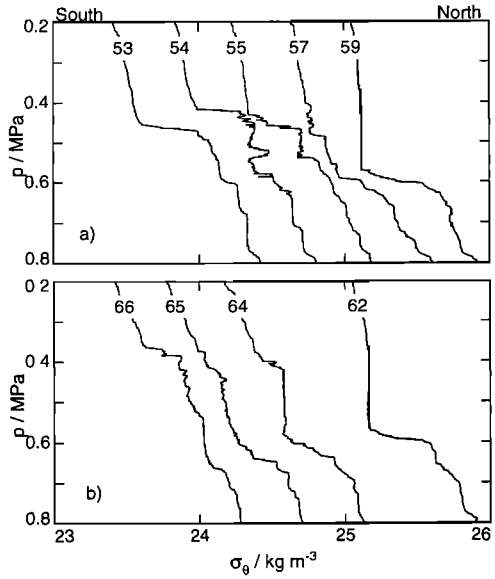

Figure 2. A series of density profiles collected in the set of billows on (a) the downstream leg, soon after the billows form, and (b) the upstream leg, several buoyancy periods later. Numbering indicates the AMP profiles plotted. The profiles are ordered by position in the billows-following reference frame, so that the large-scale density structure can be compared. The profiles are offset by 0.4 σ_θ except for 62-64, which are offset by 0.8 σ_θ. In both sets the interface rises from north to south, in response to the establishment of the hydraulic control at Bush Point. The change in vertical structure between Figures 2a and 2b reflects the action of the billows, which form a mixed layer at the depth of the interface.

ways at least weakly turbulent, neither L_b nor $L_{\rm rms}$ is ever zero. Nevertheless, the shear instability event is 5-10 times the background and is nicely bounded at 0.3 and 0.65 MPa, pressures where background turbulence and overturning are minimal. We will assume this choice of vertical boundaries justifies neglecting the vertical advection of turbulent energy at a specific horizontal position in the billows-following coordinate system. However, we cannot assume a local balance of the mean energy quantities because we have not used isopycnals or streamlines to define the vertical boundaries.

We initially performed the energetics analysis for an isopycnal-bounded control volume, selecting isopycnals where turbulent activity was at a minimum. Isopycnals are appealing bounds because advective fluxes across them are negligible; if they are also minima in average turbulent activity, then diapycnal fluxes are negligible as well. However, both the thickness and vertically averaged density varied significantly and systematically within the isopycnal-bounded sampling volume. This variability is important for two reasons. First, estimates of potential energy are very sensitive to the layer thickness, even in three-dimensional numerical simulations where the full density field is known (K. B. Winters, personal communication, 1993). When considered as a spatial series, our profile-based estimates of potential energy reflect principally the thickness change, showing no obvious signal due to mixing. Second, these changes must result from horizontal divergences or nonlocal forces (pressure-work terms). We therefore cannot assume a local mean energy balance, even when isopycnal bounds are used. We present our findings for a pressure-bounded layer because (1) the final results are very similar using either isopycnal or pressure bounds, (2) the interpretation of the observations as an Eulerian spatial series is much more straightforward when pressure bounds are used, and (3) a local balance of mean energy could not be justified using either vertical or isopycnal bounds.

2.4. Profile Groupings

Figure 4a shows the ship track within the control volume for drops 53–66. The coordinates within the box are aligned with the geographic coordinates, y positive to the north, x positive to the east. For $1 < y < 1.7$ km there are two sets of four profiles, AMPs 53–56 and AMPs 63–66, collected roughly an hour apart, which sample similar positions within the box.

Changes in the vertically averaged density within the sampling volume (Figure 4b) provide additional evidence that Figure 4a is a billows-following coordinate system. We define ρ_p for each AMP profile as the verti-

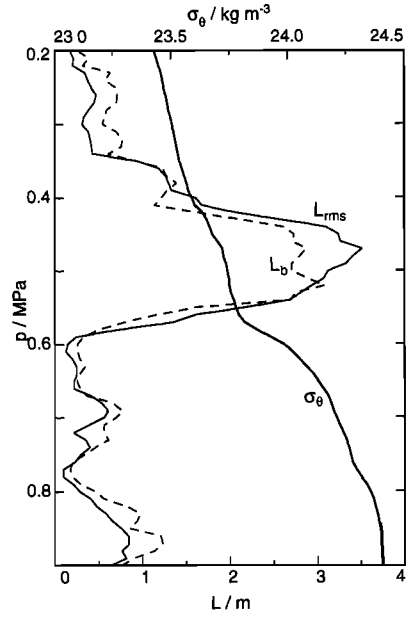

Figure 3. Average profiles of root-mean-square displacement $L_{\rm rms}$, buoyancy scale L_b, and density σ_θ using AMPs 54–66. The broad maximum between 0.4 and 0.6 MPa is the signature of the shear instability. We examine the energetics of the fluid between 0.3 and 0.65 MPa. We choose these bounds owing to minima in overturning scales at these depths, justifying neglect of vertical transport terms in the turbulent energy balance equations.

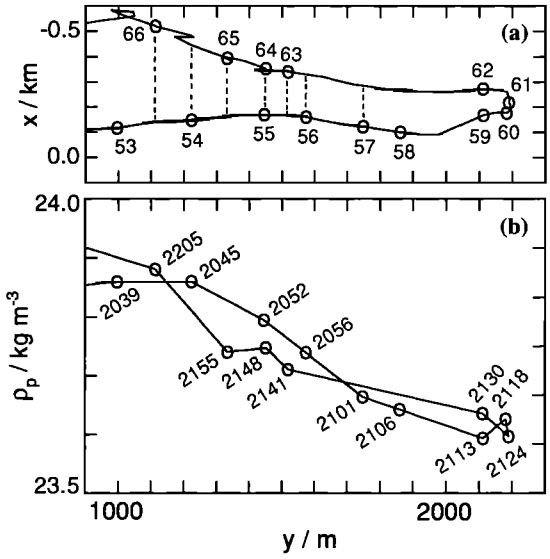

Figure 4. (a) Downstream (53–60) and upstream (61–66) ship tracks within the sample volume, when drops sampled active billows. Circles are x, y positions of AMP profiles, labeled with drop numbers. Dashed lines mark locations where conditions are compared. (b) Vertically averaged density ρ_p versus y position in the Lagrangian coordinate system showing the similarity in average density as a function of y between passes. Times when the profiles were collected are in UTC.

cally averaged density between 0.3 and 0.65 MPa. Decreasing ρ_p with increasing y is seen in both passes through the sampling volume. No systematic cross-channel (x) variations in ρ_p are apparent between the two passes. We therefore match profiles from the two passes by downstream (y) distance.

Because only one pair of profiles was taken at the same y (Figure 4a), we match a profile from one pass with a pair of profiles from the other pass that bound the same y position. The seven downstream locations chosen are shown on Figure 4a by vertical dashed lines; the drop numbers and average time between the samples are given in Table 1. From the average density profile (Figure 3) the buoyancy frequency is $N \approx 0.01$ rad s^{-1}. Using this value of N, the time difference between profiles is $N\Delta t/2\pi = 3.5 - 8.1$ buoyancy periods. The weighted average time (e.g., $\text{time}_{\text{avg}} = 0.5(\text{time}_{5866} + 0.5 \times \text{time}_{5853} + 0.5 \times \text{time}_{5854})$) at which each set of profiles was collected is the same. However, because billows developed first at the north end of the sample volume, groupings from larger y sampled the billows at a later stage of their evolution than those groupings from smaller y.

Figure 5 shows some of the grouped density and velocity profiles from Table 1. Both the instantaneous and sorted density profiles (see section 3.1) are shown, and underlines mark the beginning profile in a group. The decrease in density at 0.5 MPa moving to larger y is obvious. As expected, the earlier profile displays large density and velocity gradients near 0.5 MPa, and the later profiles show either a thick well-mixed region or a much weaker and thicker gradient region. This qualitative picture of the impact of the shear instability on the mean fields is as expected from laboratory and numerical studies.

Table 1. Profile Groupings Used in the Energetics Analysis

Primary Drop	Drop Pair	y, m	Δt, s
66	53, 54	1138	4992
54	65, 66	1248	4498
65	54, 55	1358	4009
55	64, 65	1470	3389
64	55, 56	1475	3360
63	55, 56	1544	2815
56	62, 63	1599	2641
57	62, 63	1773	2168

Variables are y, downstream position, and Δt, the time interval between collection of the primary drop and the drop pair.

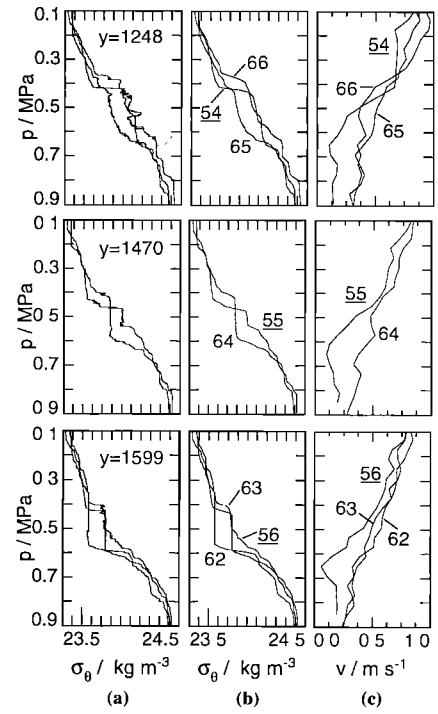

Figure 5. Three of the profile groupings used in the energetics analysis, with the profile collected on the downstream leg underlined. (a) Unsorted salinity, (b) sorted salinity, and (c) velocity profiles; y is the downstream position in the Lagrangian coordinate system. The profiles at 1248 and 1599 m show the three profiles used in typical groupings; the profiles from 1470 m are the two profiles that did not require interpolation. Earlier profiles have strong salinity and velocity gradients near 0.5 MPa that are much weaker in the later profiles.

3. Balance Equations

The energy balance of the baroclinic flow in an incompressible, stratified control volume V (in watts per kilogram) is described by [after *Monin and Yaglom*, 1971; *Gregg*, 1987; *Winters et al.*, 1995]

$$\frac{\partial}{\partial t}KE = -\nabla \cdot \mathbf{J_k} - P \tag{1}$$

$$\frac{\partial}{\partial t}TKE = P - <\epsilon> + J_b \tag{2}$$

$$\frac{d}{dt}E_b = \underbrace{-\frac{1}{\rho_0 C}\oint g\psi\vec{u}\cdot\hat{n}dC}_{\Phi_C} + \underbrace{\frac{1}{\rho_0 V}\int_V g\kappa z_* \nabla^2\rho dV}_{\Phi_d} \tag{3}$$

and

$$\frac{d}{dt}E_a = \underbrace{\frac{1}{\rho_0 V}\int_V g\rho w dV}_{-J_b} - \Phi_d - \left(\frac{1}{\rho_0 C}\oint gz\rho\vec{u}\cdot\hat{n}dC + \Phi_C\right) \tag{4}$$

where

$$TKE \equiv <0.5(u'^2 + v'^2 + w'^2)> = <0.5(q^2)> \tag{5}$$

$$P \equiv < -\overline{u'w'}(\partial u/\partial z) - \overline{v'w'}(\partial v/\partial z) > \tag{6}$$

$$\psi \equiv \int^{\rho} z_*(\hat{\rho})d\hat{\rho} \tag{7}$$

and

$$<> \equiv \frac{1}{V}\int_V dV \tag{8}$$

Here KE is the mean kinetic energy, defined below; TKE is the turbulent kinetic energy; E_b is the background potential energy; E_a is the available potential energy; P is turbulent production, coupling (1) and (2); and J_b is the buoyancy flux, coupling (2) and (4). Turbulent velocity fluctuations are denoted with primes; q is the turbulent velocity scale; z_* is a sorting index (see section 1); ρ_0 is a reference density; κ is the diffusivity of mass; C is the volume surface; and g is gravitational acceleration. The divergence of the energy-flux density vector in (1), $\nabla \cdot \mathbf{J_k}$, accounts for unresolved energy-flux divergences, due to advection of KE or pressure work (diffusion is assumed negligible). This divergence can be a dominant term in the equation if nonlocal processes are important to the dynamics. In (1) we make the standard assumptions that the viscous dissipation by the mean currents and the buoyancy flux due to the mean currents are negligible, and in (2) we assume a local, time-dependent balance.

Equations (1) and (2) are standard forms for the kinetic energy balance equations assuming a Reynolds decomposition. Equations (3) and (4) are balance equations for potential energy suggested by *Winters et al.* [1995] which rely on a three-dimensional sorting of the density field to define the components of the potential energy. This decomposition clearly identifies E_b as the only component that changes due to diabatic processes. K. B. Winters and E. A. D'Asaro (Diapycnal fluxes in density-stratified flows, submitted to *Journal of Fluid Mechanics*, 1994) have shown that Φ_d, the conversion of E_a to E_b, is equal to the volume-integrated value of $0.5\ \chi_{pe}$, the rate of dissipation of potential energy fluctuations. (The scaling factor of 0.5 arises solely from our definition of χ [see *Seim and Gregg*, 1994, equation (1b)]. Historically, χ has been defined as 2 times the integrated thermal gradient variance, though definitions vary.) Further, (3) demonstrates that Φ_d is always directly related to the change in E_b, whereas (4) shows that the buoyancy flux is only indirectly related to changes in E_b. Only when E_a is steady does the buoyancy flux equal Φ_d.

The term Φ_C in (3) is the net advective flux of background potential energy into the control volume. There is an analogous term in (4) for the flux of available potential energy. The inclusion of these terms generalizes the theory to account for open systems.

Unfortunately, there is no way to estimate the terms in (3) and (4) with the one-dimensional profiles we collected. Instead, we use approximate forms of the equations (in watts per kilogram) based on one-dimensional data:

$$\frac{\partial}{\partial t}BPE = -\nabla \cdot \mathbf{J_p} + 0.5\chi_{pe} \tag{9}$$

$$\frac{\partial}{\partial t}APEF = -0.5 \times \chi_{pe} - J_b \tag{10}$$

where

$$APEF \equiv <0.5[g/(\rho N)]^2\overline{\rho'^2}> \tag{11}$$

$$\chi_{pe} \equiv <(g\alpha/N)^2(1 + 1/R_\rho^2)\chi> \tag{12}$$

Here BPE is a one-dimensional estimator of the background potential energy, defined below; $APEF$ is the available potential energy of fluctuations; χ_{pe} is an estimator of Φ_d; α is the thermal expansion coefficient; $R_\rho \equiv \alpha(\partial T/\partial z)/\beta(\partial S/\partial z) \approx -0.05$ is the stability ratio; and β is the haline contraction coefficient. The term $\nabla \cdot \mathbf{J_p}$ is an energy flux divergence that represents the advective flux divergence and buoyancy flux due to mean (nonturbulent) motions. As with (1), this term may be large if there is a net transport of potential energy into or out of the control volume. A local, time-dependent balance is assumed in (10).

Together, (1), (2), (9), and (10) form a set of consistent relations that describe the energy budget; that is, when summed, they show that energy changes of the baroclinic flow are due to either flux divergence or viscous dissipation. These equations describe the energy balance during an instability. Energy accumulates in the volume by flux convergence until the KE exceeds the work needed to overturn the density field. Energy is then lost to turbulent production, with P being the source term for (2); energy is then either stored

as TKE, dissipated via ϵ, or converted to available potential energy through J_b. Finally, $APEF$ may be converted to BPE through χ_{pe}. We will use our observations to estimate the magnitude of the various terms.

We have intentionally left out the energy components of the depth-averaged flow in our development; that is, we do not address the energy budget of the barotropic flow. We assume that the kinetic energy due to the vertically averaged flow $\overline{KE}$ and potential energy due to the vertically averaged density $\overline{PE}$ do not directly act as sources or sinks for the shear instability and therefore exclude them from the energy balance. Though the variations in these components are important to understanding the forcing and structure of the billows, our observations are inadequate to address the energetics of the barotropic flow. In particular, we do not have a measure of the free-surface gradient that is typically a dominant term in the barotropic energy budget. To examine the forcing of the instability, we define the total (barotropic + baroclinic) energy (minus the free-surface gradient) as

$$TE \equiv \overline{KE} + KE + \overline{PE} + BPE \tag{13}$$

but when analyzing the energetics of the billows, we consider only the mean energy of the baroclinic flow, KE and BPE.

Our definition of the mean and turbulent velocity components in this study is set by the structure of the flow. We use the ADCP profiles for the mean velocity. These data resolve vertical scales greater than 12 m and are horizontally averaged over approximately 60 m, roughly a wavelength of the instability. Because they are averaged for only 2 min in time, they include tidal and internal-wave contributions with scales larger than 60 m, as well as the time-mean, baroclinic currents. Turbulent motions are measured by the shear probes on AMP at scales from 0.01 to 1 m, hence there is a distinct scale separation.

When estimating KE (in joules per kilogram), we first remove the vertically averaged velocities,

$$KE = \frac{1}{\rho_0 d}\int_{z_l}^{z_u} \rho/2[(u-\overline{u})^2 + (v-\overline{v})^2]\, dz \tag{14}$$

where $\overline{u}$ and $\overline{v}$ are the average east and north velocities, respectively, between $z_u = -30$ m and $z_l = -65$ m for each profile, and $d = z_u - z_l$. The average of ρ_p for profiles 53–66 is ρ_0. We assume the mean vertical velocity w is small compared to u and v. The demeaned velocities are used because only the kinetic energy due to the depth-varying current is a source of energy for a shear instability. On the basis of the rms error of the velocity estimates, uncertainty in KE is $\pm 2 \times 10^{-4}$ m^2 s^{-2}.

There is not a natural scale separation of the density measurements. Rather than decomposing the density field by horizontal averaging, the AMP density profiles are decomposed into background and available components using a sorting algorithm developed by *Thorpe* [1977]. The density values from each AMP profile are sorted to increase monotonically with pressure, the minimum energy state achievable with the values. The stable profile is a measure of the background density field. The difference between the observed and sorted profiles is the available density component. This is a one-dimensional version of the sorting algorithm used by *Winters et al.* [1995], and it is common in microstructure studies to use the sorted density profile to define the stratification against which overturns are straining. The sorting leads to the following decomposition of each density profile:

$$\rho(z) = \rho_p + \hat{\rho}(z) + \rho'(z) \tag{15}$$

where $\hat{\rho}(z)$ is the (demeaned) sorted density profile and ρ' is the density fluctuation of static instabilities.

As with KE, we first remove the vertically averaged component of the density before forming the background potential energy (in joules per kilogram)

$$BPE = \frac{g}{\rho_0 d}\int_{z_0-d/2}^{z_0+d/2} \hat{\rho}(z) z\, dz \tag{16}$$

where $z_0 = 0.5(z_l + z_u)$. The background potential energy reflects the stratification within the control volume. It is negative definite and approaches zero as $\hat{\rho}$ goes to zero (i.e., the density becomes uniform).

There are two sources of uncertainty in BPE. One source is errors in our measurement of ρ. On the basis of the small spread of density values on a temperature-salinity plot, errors in ρ are small; we estimate $\pm 0.024\%$ uncertainty. The other source is the unaveraged nature of the measurement; that is, density values along an AMP profile are point samples, unlike the ADCP profiles which are averaged over 60 m. Variability in BPE within the large-scale structures is large. On the basis of the variations in BPE in a set of four profiles (59–62) collected in approximately the same location at the north end of the sampling volume (Figure 4a) we ascribe $\pm 10\%$ uncertainty to BPE owing to the unaveraged nature of the estimate.

We next briefly mention how we form ϵ, TKE, $APEF$, and χ_{pe} and state their uncertainties. We simply average ϵ between 0.3 and 0.65 MPa for each profile. Errors in ϵ are difficult to quantify (see part 1); we conservatively estimate error bounds of a factor of 2.

The shear probes cannot be used to directly measure TKE because AMP's motions contaminate the measured velocities at scales larger than approximately 1 m. We therefore estimate q by two methods to confirm the validity of the estimators. The appendix details the methods used and the comparison. On the basis of the average difference between the two estimates we assume error bounds of $(0.75, 1.33)q$.

Gregg [1987] calls $APEF$ the specific fluctuation potential energy; the values from (11) are very similar to the available potential energy of fluctuations proposed by *Dillon and Park* [1987]. Total uncertainty in $APEF$ is $\pm 6\%$, most of which is due to 5% errors in N^2.

We only indirectly measure χ_{pe}. The dissipation rate of temperature variance χ is determined from temper-

ature gradient spectra measured with glass-bead thermistors, but the dissipation rate of salt χ_s cannot be measured because its viscous-diffusive subrange occurs at very small scales. Following *Gregg* [1984], we assume the two dissipation rates are proportional to the square of their respective contributions to the mean vertical gradient that leads to (12). Because $R_\rho = -0.05$, salinity stratification is 20 times temperature stratification, indicating χ is only 5% of χ_{pe}. *Wijesekera et al.* [1993] propose an alternate method of computing χ_{pe} based on ϵ and the level of the 5/3rd moment density spectrum in the inertial subrange. Applying this technique to the large overturns in the mixing layer yields estimates within a factor of 2 of our χ-based estimate. Consequently, we assume a factor of 2 uncertainty in χ_{pe}.

The time difference used in computing derivatives is determined by the trajectory shown in Figure 4b; hence errors in the trajectory set the level of uncertainty of the time derivatives. Random errors in velocity introduce approximately 2% error in positions. Errors in tracking depth produce a bias error that varies strongly with vertical position. Trajectories formed at 0.47–0.53 MPa alter the time differences by a few percent at most, but trajectories formed at 0.4 or 0.6 MPa are much different and lead to different drop pairings. We use the velocities at 0.5 MPa because they minimize differences in density between the downstream and upstream legs. An additional 5% uncertainty is assumed to result from errors in time difference when computing derivatives.

4. Data

Using AMPs 49–58, the downstream section through Bush Point, we first examine energy changes in an Eulerian frame of reference before the billows form to understand how the instability is forced. Observations to be used in the energy balance are then presented in the billows-following coordinate system.

4.1. Forcing

Figure 6 displays all the measured quantities, starting upstream of the hydraulic control, as a function of geographic position. The coordinate system is Eulerian, corresponding to the distance axis in Figure 1. The left-hand panels show the breakdown of total mean energy, including the vertically averaged component; the right-hand panels show the components used subsequently in the energetics analysis. Total mean energy in the

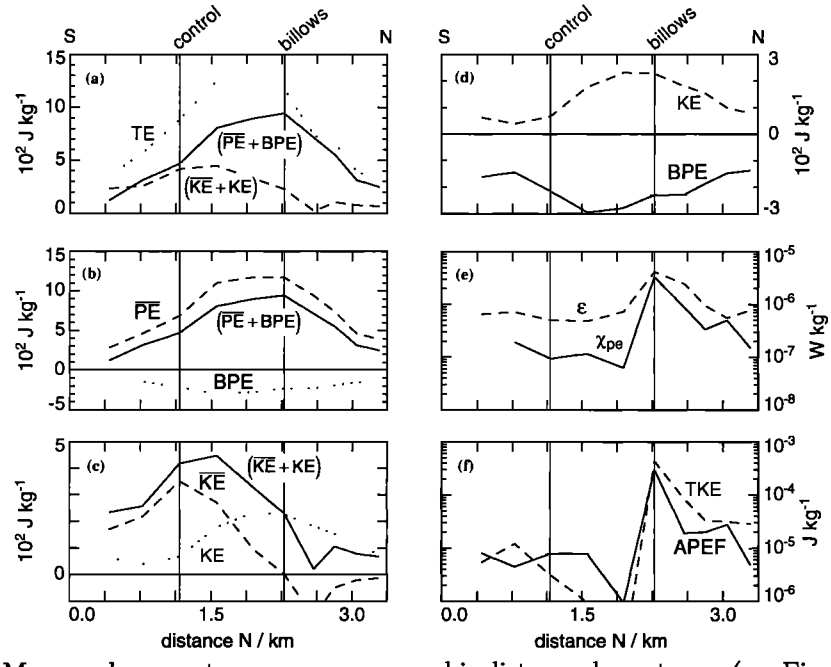

Figure 6. Measured energy terms versus geographic distance downstream (see Figure 1), showing the rapid increase in mean energy upstream of the billows and sudden increase in turbulence as the billows form. Vertical solid lines mark the location of the hydraulic control and where billows first appear. (a) The total energy TE breakdown shows the dominance of (b) potential energy of the vertically averaged flow $\overline{PE}$ and (c) kinetic energy of the vertically averaged flow $\overline{KE}$. Right panels show terms used to evaluate the energy balance. (d) Kinetic energy of the depth-varying flow KE peaks as the billows form and subsequently decreases; background potential energy BPE is a mirror image of KE. (e) Dissipation rates and (f) turbulent energy increase dramatically as the billows form.

sample volume, $TE \equiv \overline{KE} + KE + \overline{PE} + BPE$, begins rising upstream of the control, reaching a plateau between the control and where large billows form (Figure 6a). Upstream of the control, the energy changes are dominated by $\overline{KE}$ and $\overline{PE}$ (Figures 6b and 6c), reflecting the increased depth-averaged speed and depth-averaged density ρ_p of the control volume entering the contraction. The increase in ρ_p results from the rising density interface, and the increase continues downstream of the control until the billows form (Figure 7).

The rising interface also increases the density gradient, causing BPE to decrease (Figure 6d). The rapid decrease of BPE before the billows form highlights the role of advective flux divergence in forcing the onset of instability (Figure 6).

Downstream of the control, $\overline{KE}$ decreases but KE increases, reaching a maximum just before the billows form (Figure 6d). The coincidence of peak KE with billows formation suggests it ultimately destabilizes the shear layer.

The magnitudes of TKE and $APEF$ upstream of the billows are only 0.1% of the variations in KE and BPE (Figures 6d and 6f). Dissipation rates, however, are not small, ϵ averaging 5×10^{-7} W kg^{-1}, χ_{pe} about 0.2ϵ.

The first profile through the billows finds all the turbulent fields vastly increased (Figure 6e); all achieve maximum values in this profile. All variables, save BPE, then decrease through the end of the section. Changes in KE and BPE are nearly mirror images (Figure 6d). The decrease (increase) in KE (BPE) after the billows form is consistent with it being a source (sink) of energy for the instability. A decrease in ϵ is expected for a growing shear layer. For a self-similar flow, scaling suggests $\epsilon \propto 1/h$, where h is the vorticity thickness, the product ϵh remaining constant downstream of the point where self-similarity is achieved [*Tennekes and Lumley*, 1972; part 1].

In summary, as the flow entered the hydraulic control, total energy in the sample volume increased sharply. Using 0.4 m s^{-1} for the depth-averaged speed of the volume, the change in TE required an energy flux into the sample volume of 2.8×10^{-5} W kg^{-1}. The increase was greatest in $\overline{KE}$ and $\overline{PE}$; the rate of increase of KE over the same distance was 4×10^{-6} W kg^{-1}, much less than for TE, and was entirely offset by the decrease in BPE. As soon as the billows formed, both TKE and $APEF$ increased dramatically, as did ϵ and χ_{pe}. Decreasing KE and increasing BPE after the billows formed is consistent with energy transfers expected of a shear instability.

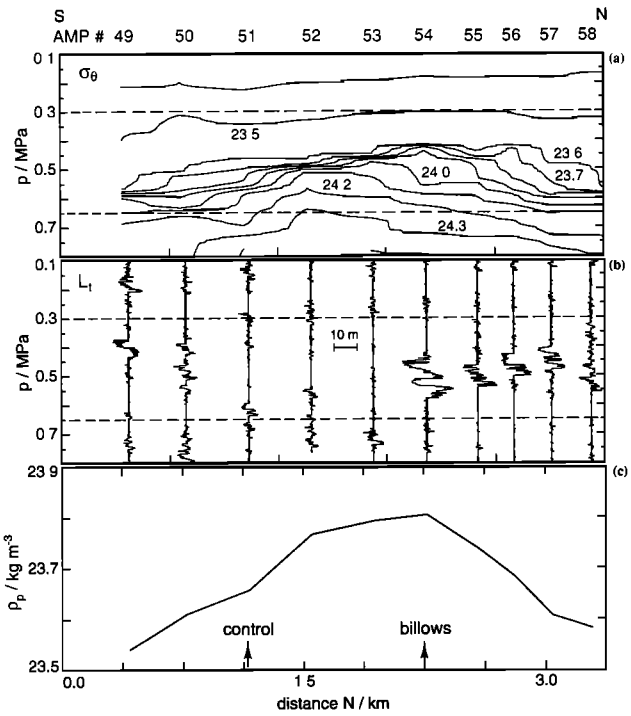

Figure 7. (a) Contour plot of density σ_θ as a function of geographic position, (b) profiles of vertical displacement L_t, and (c) vertically averaged density ρ_p in the sample volume. Isopycnals rise prior to the billows, causing an increase in ρ_p (and $\overline{PE}$). Vertical boundaries of the sample volume (dashed lines in (a) and (b)) do not cut through the large overturns; we therefore assume a local turbulent balance.

4.2. Data in the Billows-Following Coordinate System

We next consider samples collected while the billows are actively turbulent. Simple trends appear when the data are plotted against y in the billows-following reference frame (Figure 8). The regular increase of BPE (Figure 8a) and decrease of KE (Figure 8d) in the downstream leg indicate a persistent transfer of kinetic to potential energy. On the upstream leg, KE and BPE are roughly constant; all these profiles were collected about the same geographic distance downstream of the hydraulic control (Figure 1). The constancy of the mean energy values suggests the billows are spatially growing.

Neither $APEF$ nor TKE exhibit consistent patterns in the Lagrangian coordinate system (Figures 8b and 8e). The pronounced spikes in $APEF$ for AMP 54 and 62 look suspect; however, these drops appear to sample pairing events (part 1). Pairing may be the principal mechanism of entrainment and growth of a shear layer [*Ho and Huerre*, 1984]. Turbulent potential energy maxima are likely during these events that incorporate large volumes of nonturbulent fluid into the shear layer.

Dissipation (Figures 8c and 8f) is greatest to the south, being roughly a factor of 10 smaller at the north end of the set of billows, during both the downstream and upstream legs. The increased dissipation at small y in the Lagrangian coordinate system is probably related to the decreased offset of the velocity and density interfaces (part 1). The interface offset leads to significant variations in the turbulent properties of the billows, as well as their mean density.

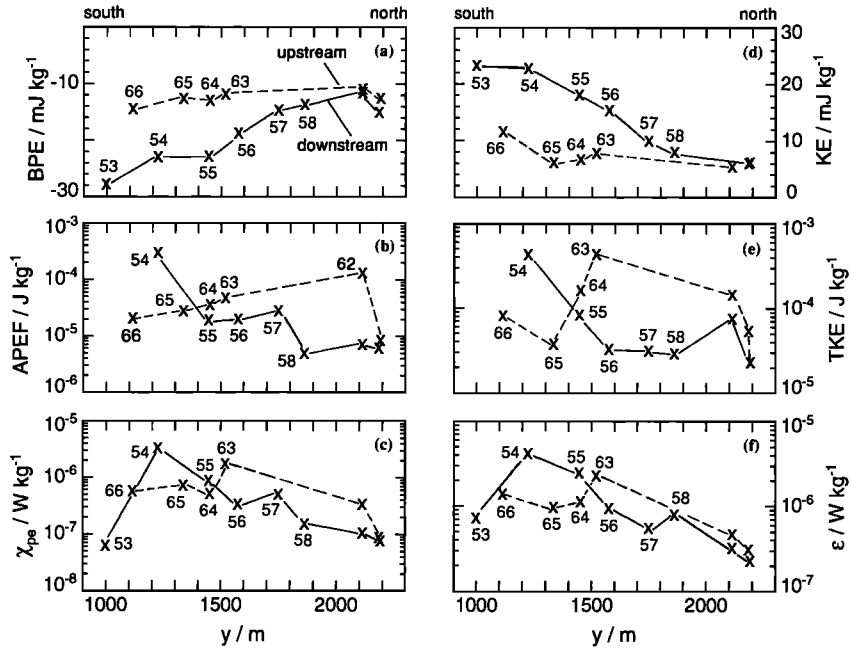

Figure 8. Measured components in the billows-following reference frame. A solid line connects profiles collected on the downstream leg, and a dashed line connects profiles collected on the upstream leg. AMP drop numbers are given. Terms in the PE balance are to the left, KE terms are to the right. (a),(d) The increase (decrease) in BPE (KE) between the upstream and the downstream legs diminishes as the time difference between the sampling decreases. (b),(e) The available potential energy of fluctuations $APEF$ and the turbulent kinetic energy TKE display no obvious trends, and for AMP 53 are less than the minimum value on the graph. (c),(f) From AMP 54 on, both χ_{pe} and ϵ tend to be largest for smaller y; this probably reflects the decreasing vertical separation of the velocity and density interfaces with decreasing y (see part 1).

5. Results

5.1. Estimated Terms

We estimate unmeasured terms using the balance equations of section 3 for each of the profile groupings (section 2.4). For each group of AMP drops in Table 1, we (1) find two values of each measured variable at the same y location, one from the primary drop and the second from interpolating between the bounding drops; (2) approximate derivatives in the energy balances by first-differencing the two values, $\partial X/\partial t \approx \Delta X/\Delta t$, and average other terms; and (3) estimate the unmeasured terms by first solving (10) for J_b and (2) for P, then computing the energy-flux divergences from (1) and (9).

The results are presented in Figure 9 as a function of y in the billows-following coordinate system. Each panel displays the balance of terms for an equation. The term being solved for is marked by a dashed line, and confidence limits are shown by shading.

Equations (2) and (10) are practically steady; both $\partial APEF/\partial t$ and $\partial TKE/\partial t$ are an order of magnitude smaller than the other terms (Figures 9a and 9b). Thus these two turbulent energy equations (in watts per kilogram) simplify to approximately steady, local balances,

i.e.,

$$J_b \approx -\chi_{pe}/2 \approx -5.5 \times 10^{-7}$$

and

$$P \approx \epsilon - J_b \approx 2.4 \times 10^{-6}$$

averaged over all pairs. Confidence limits for P are somewhat less than a factor of 2 owing to a correlation coefficient of 0.91 between ϵ and J_b. Both J_b and ϵ tend to decrease to the north, as does P, reflecting the increasing separation of the velocity and density interfaces (part 1).

The mean energy balance equations are not steady because the time derivatives are the largest terms in the balance equations; (1) simplifies to

$$\partial KE/\partial t \approx -P$$

with P, on average, accounting for 87% of the change in KE. We find that $\nabla \cdot \mathbf{J_k}$ is not significantly different from zero, implying a nonsteady, local balance adequately describes the mean kinetic energy budget in the billows-following coordinate system. This is consistent with the laboratory study of *Thorpe* [1973a]; he estimated only 5% of the energy released by shear instabilities contributed to the generation of propagating internal waves.

The BPE budget does not simplify to a local balance. Though $\partial BPE/\partial t$ is positive for all the estimates, which is consistent with BPE being a sink for turbulent energy, on average, the $0.5 \times \chi_{pe}$ term accounts for only 25% of the changes in BPE. Given the

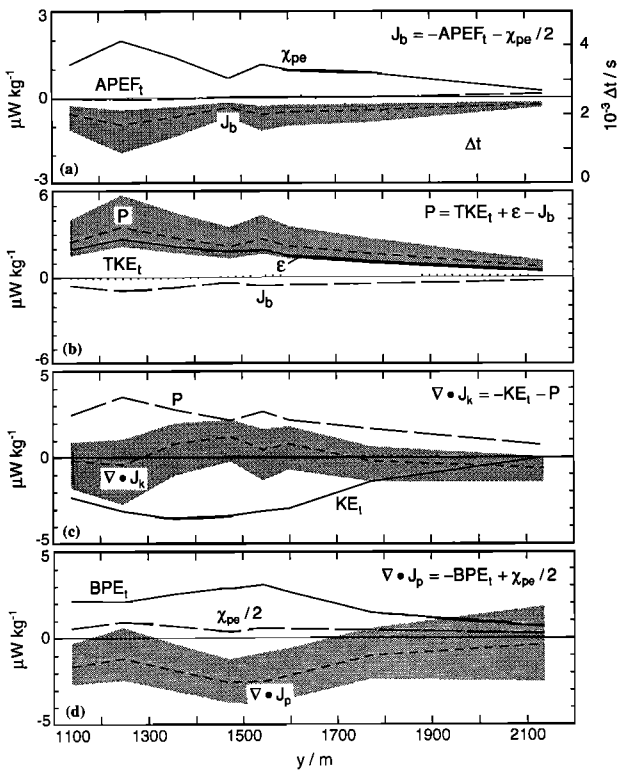

Figure 9. Plot of terms in each of the four balance equations. In each panel the term solved for is shown with a dashed line, and shading marks confidence limits for the estimates. (a),(b) The turbulent energy equations simplify to steady local balances owing to consistently small values of $\partial TKE/\partial t$ and $\partial APEF/\partial t$. The differencing time Δt of each grouping is shown in (a). (c) The KE flux divergence $\nabla \cdot \mathbf{J_k}$ is not significantly different from zero, implying a nonsteady local balance of KE, but the same is not true (d) for BPE where the BPE flux divergence $\nabla \cdot \mathbf{J_p}$ is a dominant term.

approximate local balance of KE, this result is surprising. There are at least three possible reasons for the discrepancy: first, our one-dimensional estimates of BPE may inadequately isolate diabatic processes; second, we may have undersampled the dissipation; and third, our use of χ to represent χ_{pe} may be inappropriate. These possibilities are discussed below.

5.2. Implications

We estimate the flux Richardson number, $R_f \equiv J_b/P$, to be 0.22 ± 0.1 over the event, where 0.05 is 1 standard deviation. Individual values vary between 0.16 and 0.33. Our average R_f is close to the maximum value found in laboratory experiments studying buoyancy-affected shear layers [*Thorpe*, 1987], where maximum values are associated with an initial $Ri \approx 0.05$. *Thorpe* [1973b] found billows to have a low mixing efficiency for near-critical Ri flows and a final state of nearly linear transition of density across the shear layer but voiced suspicions that his laboratory results may not be applicable to large Re flows. The high mixing efficiency and formation of a well-mixed layer in this event support his suspicion that mixing efficiency may be a function of Re.

Most laboratory estimates of mixing efficiency compare initial and final mean kinetic and mean potential energies. For this data set we find the ratio of BPE change to KE change is 0.86, much larger than our estimate of R_f based on the microstructure measurements or any previous estimates. Use of this formulation, however, requires a local mean energy balance, which we cannot demonstrate for BPE. Obviously, great care must be exercised when evaluating the mixing efficiency from changes in the mean fields without the benefit of microstructure measurements.

Finding (1) to be in local balance implies the billows do not generate radiating internal waves, at least in this study. Because the billows are moving relative to the surrounding fluid, they induce vertical motions in the fluid around them, similar to an obstacle effect. These vertical oscillations force propagating internal waves if the horizontal wavenumber of the billows k is less than N/U, where U is the speed of the surrounding flow relative to the billows [*Gill*, 1982]. The waves can carry momentum away from the shear layer; a similar process has been proposed to explain the diurnal cycle of turbulence beneath the mixed layer observed on the equator [*Gregg et al.*, 1985; *Wijesekera and Dillon*, 1991]. A large internal-wave momentum flux would significantly alter the energy balance by reducing the amount of KE released by the instability available for turbulent production P.

Using $N = 10^{-2}$ rad s^{-1} and $U = 0.2$ m s^{-1} (half the speed difference between layers) yields $k = 0.05$ rad m^{-1}. Billows of horizontal wavenumber greater than 0.05, or wavelengths less than 125 m, will generate evanescent modes that are incapable of carrying energy away from their source. The observed billows' wavelength of 70 m is much less than the critical value, so vertical oscillations at this horizontal scale in the surrounding fluid decrease exponentially with distance from the shear layer and are incapable of carrying energy. This is consistent with the acoustic images (part 1) that show wave-like oscillations on the scattering layers surrounding the billows whose phase lines are vertical.

Fritts [1979, 1984] promotes an envelope radiation mechanism as an efficient way to remove momentum from an unstable free shear layer. The envelope radiation mechanism generates freely propagating internal waves as flow moves past an irregular flow feature characterized by spatial variations at a wavenumber less than that of the billows. *Fritts* [1979, 1984] assumes the presence of two trains of Kelvin-Helmholtz billows, with similar wavenumbers, which have a beat wavenumber $k_b \ll k$. Because we see no evidence of internal-wave radiation, we presume that this mixing event is poorly described as the sum of two wave trains.

At least three factors may account for the lack of a local, nonsteady balance of BPE. The first concerns the sorting algorithm used to define the background density

field. When performed in three dimensions over the entire domain, as in a numerical simulation, the sorting clearly defines a configuration of the density field that can be changed only by mixing [*Winters and D'Asaro*, 1994; *Winters et al.*, 1995]. The one-dimensional sort possible with profiles is only an approximation of a three-dimensional sort. In particular, instantaneous estimates of BPE within a volume based on sorted profiles can vary due to adiabatic processes; the variability of BPE in profiles 59–62 (Figure 8) is evidence of this effect. We included an energy-flux divergence in the balance equation for BPE in recognition of the sensitivity of our BPE estimates to adiabatically induced changes. Thus finding a nonlocal balance of BPE is not unexpected. It is a surprise, however, to find a local balance for KE because the internal waves assumed to carry the energy flux should have a signature in both potential and kinetic energy. The consistency of BPE and its changes over time suggest that the profiles reflect large-scale changes in BPE, rather than small-scale, wave-induced variability.

Another possibility is that we underestimate the event-averaged dissipation rate. Our analysis estimates the average dissipation rates over the lifetime of the event from two measurements widely separated in time. Because of their highly skewed distributions, both ϵ and χ_{pe} tend to be underestimated by small-sample means [*Gregg*, 1987]. The large error bounds of these variables used in the analysis reflect the sampling problem associated with variables that are approximately lognormally distributed. We do not think we grossly underestimate the true event-averaged values because the maximum likelihood estimate of 2×10^{-6} W kg^{-1} based on the 0.5-m values is very close to the arithmetic mean.

Nevertheless, uncertainties in both variables are large; if we assume P and J_b are underestimated by a factor of 1.7 (within the stated confidence limits), both the KE and the BPE budgets require an energy flux convergence of $\approx 1.35 \times 10^{-6}$ W kg^{-1}. This value seems plausible and also resolves the discrepancy between the potential and kinetic energy balances, by requiring a moderate nonlocal source of energy to close the balances for both. This scenario suggests energy was supplied to and consumed by the shear layer after billows formed. Conversely, assuming we have overestimated the dissipation rate by a factor of 1.7 requires $\nabla \cdot \mathbf{J_k} \approx 1.5 \times 10^{-6}$ W kg^{-1} and $\nabla \cdot \mathbf{J_p} \approx -2.1 \times 10^{-6}$ W kg^{-1}, that is, half the change in KE is lost to wave radiation, while almost all of the increase in BPE is due to a convergence of potential energy flux. It seems unlikely that the energy-flux divergences would be large and of opposite sign, and more fundamentally, that we may consistently overestimate the dissipation rates, though we do not have a definitive reason to discount this possibility.

Lastly, the errors associated with using χ to infer χ_{pe} in a dominantly salt-stratified fluid are unknown. The dissipation rate of salt χ_s remains unmeasured owing to the extremely small scales at which salt diffuses. If χ and χ_s are not strongly correlated spatially, our estimator is ill posed. More practically, conditions in Puget Sound at this time were not ideal for our instrumentation; the weak mean thermal gradient and large values of ϵ combined to produce a temperature gradient spectrum at the limit of our ability to resolve.

5.3. Interfacial Stress

Having established that (2) is approximately steady in time, we can readily form an estimate of the turbulent shear stress due to the mixing event. Because the billows occurred at a distinct interface in both the velocity and density fields, the shear stress is also the interfacial stress. We form

$$\rho\overline{v'w'} = \frac{-\epsilon}{(1 - R_f)\partial v/\partial z} \tag{17}$$

(in pascals) from the average profiles of v and ϵ for the AMP drops used in the groupings. The shear stress is dramatically elevated between 0.4 and 0.6 MPa, rising to maximum values of 0.32 Pa; it is, on average, 0.22 Pa over this depth range (Figure 10). This is one of the few direct estimates of interfacial stress based on multiple samples from roughly the same water mass. This stress is comparable to the maximum momentum flux in boundary layers over ice [*Overland*, 1985] and under ice [*McPhee and Smith*, 1976], suggesting this level of stress is dynamically important. It is important to note this is the average stress over approximately an hour; peak

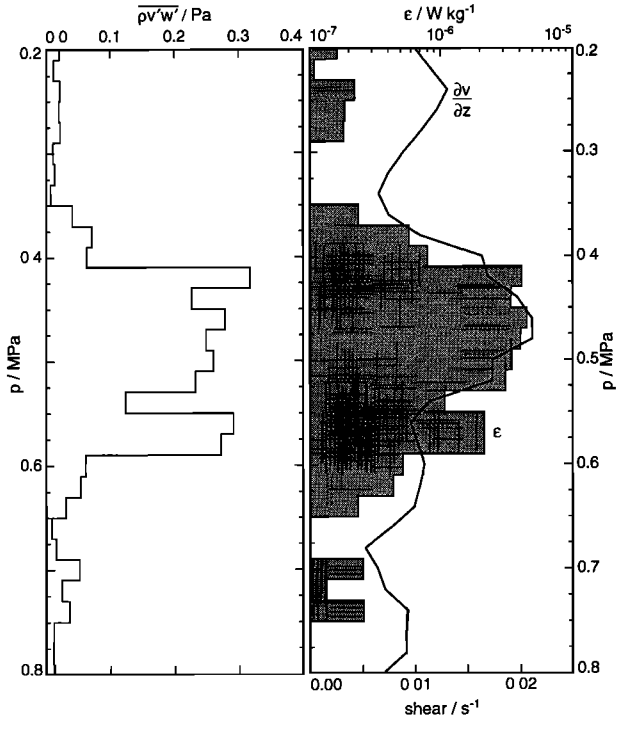

Figure 10. Average profiles of (right) ϵ and shear and (left) shear stress, based on the profiles used in the groupings. The signature of the mixing event is confined between 0.4 and 0.6 MPa and reaches maximum average values of 0.32 Pa.

values from individual profiles exceed 1.5 Pa. Unaveraged estimates of interfacial stress in the outflow of the Mediterranean based on profiles of ϵ from expendable dissipation profilers and shear from expendable current profilers are quite large, up to 2.25 Pa [*Price et al.*, 1993].

6. Summary and Discussion

6.1. Summary

We examine the changes in energy distribution within a control volume containing a large mixing event. A control volume that completely contains the mixing event and whose boundaries support relatively little turbulent mixing is selected. This justifies the use of a local balance of turbulent energy. We decompose the velocity and density fields into layer-mean and depth-varying components, assuming mixing will affect only the depth-varying components. A simple energy balance is used to quantify the role of turbulent processes, to estimate the efficiency of mixing, and to quantify the energy radiation.

Prior to instability the fluid passed through a lateral constriction that accelerated the flow to criticality. Though the increased speed resulted in a doubling of the kinetic energy, potential energy accounted for the majority of the increase. The mechanism of the increase was isopycnal uplift, associated with thinning of the upper layer as its flow became supercritical. The uplift increased the mean density and stratification of the layer. The coincident increase in shear ultimately caused the instability. Though dissipation within the control volume is not small prior to the formation of the billows, it is not associated with large-scale overturns and therefore results in little turbulent energy. We estimate the upstream turbulent velocity is less than 1% of the mean speed.

As billows formed, turbulent energy increased an order of magnitude. Kinetic energy due to shear then decreased and potential energy due to stratification increased, as expected for a shear-driven instability. Over the next hour, turbulent energy and dissipation varied widely as the ship sampled different locations within the turbulent shear layer.

When viewed in a billows-following reference frame, both ϵ and χ_{pe} decreased regularly to the north. Neither $APEF$ nor TKE exhibits simple trends in the billows-following reference frame. Two distinct maxima in $APEF$ are thought to be associated with pairing events.

We estimate unmeasured terms in the energy balance by pairing profiles that sampled approximately the same location in the billows-following coordinate system, using first differences to estimate derivatives. The analysis quantifies the magnitude of terms in a simple energy budget after coherent structures had formed and before their eventual demise. Average values from the analysis are given in Table 2. In summary, we find the following.

Table 2. Average Values of Terms in the Energy Balance

Term	Definition	Value, μW kg^{-1}
$\partial KE/\partial t$	Rate of change of KE	-2.9 ± 0.7
P	Turbulent production	2.4 ± 0.5
$\nabla \cdot J_k$	KE flux divergence	0.5 ± 0.6
$\partial BPE/\partial t$	Rate of change of BPE	2.5 ± 0.5
J_b	Buoyancy flux	-0.6 ± 0.2
$\nabla \cdot J_p$	BPE flux divergence	-1.9 ± 0.6
ϵ	TKE dissipation rate	1.9 ± 0.4
χ_{pe}	$APEF$ dissipation rate	1.1 ± 0.4
R_f	Flux Richardson number	0.22 ± 0.04*
$\partial TKE/\partial t$	Rate of change of TKE	0.04 ± 0.09
$\partial APEF/\partial t$	Rate of change of $APEF$	-0.01 ± 0.03

Values include ± 1 standard deviation.
*Value is nondimensional.

1. The TKE and $APEF$ balance equations are steady when evaluated over several buoyancy periods, such that $J_b \approx -\chi_{pe}/2 \approx -5.5 \times 10^{-7}$ W kg^{-1} and $P \approx \epsilon - J_b \approx 2.4 \times 10^{-6}$ W kg^{-1}. We estimate that, on average, $R_f \approx 0.22$ for these observations over the event.

2. We find that, on average, 87% of the change in KE is accounted for by P. Both KE and P follow similar trends, further supporting the notion that most of the observed loss of KE contributed to energizing turbulence. The small fraction of unaccounted for energy suggests that mostly evanescent waves were excited by the shear layer despite the presence of stratified fluid that surrounds the mixing event and can support internal waves.

3. The BPE budget does not close locally. The estimates of $\chi_{pe}/2$ explain about 25% of the change in BPE. The discrepancy may be due to problems with estimating BPE and χ_{pe} or to an undersampling of the dissipation rates. We consider it likely that we underestimate the dissipation rates. Increasing P and J_b by a factor of 1.7 requires an equal amount of energy-flux convergence ($\approx 1.4 \times 10^{-6}$ W kg^{-1}) for both the KE and BPE budgets to balance. This suggests there was actually an net flux of energy into the layer during the event.

4. We estimate the interfacial stress due to the shear instability to average 0.22 Pa between 0.4 and 0.6 MPa for roughly an hour.

6.2. Discussion

The mixing event we sampled was generated by a flow constriction which acts as a hydraulic control during part of the tidal cycle. Rapid flow acceleration and shear enhancement passing through the constriction destabilize the fluid layer, resulting in the forma-

tion of a kilometer-long mixing patch. Though we cannot say how common such events are, our study does suggest that abrupt topography is capable of generating significant mixing. *Geyer and Smith* [1987] noted similar behavior in the Fraser River Estuary. In steady (nontidal) flows, such as overflows of dense water from marginal seas or the passage of deep water through a constriction, a generation mechanism of this type could lead to a steady (permanent), spatially growing shear layer. Such an instability could play an important role in water-mass modification and would be an excellent site for further study of large Re shear layers.

Though we have analyzed only a single realization, we find the principal results to be quite robust. We initially tried an isopycnal-bounded control volume, rather than a fixed-depth bounded control volume, hoping to better isolate diabatic processes. Though we abandoned this approach after finding that little was gained from this complicated procedure, we arrived at the same results: a dramatic energy increase prior to instability, a near-local balance of KE but not of BPE, and large mixing efficiencies. Similarly, choosing different depth bounds changes the quantitative results little. We feel confident that our analysis provides a valid sample of a large Re, high initial Ri shear layer in a natural environment.

This instability leads to significant changes in the mean velocity and density fields and therefore is likely to be important to the dynamics of Admiralty Inlet. The turbulent momentum flux changes the velocity profile from an approximately two-layer flow to a constant shear profile; the mixing due to the event changes the density field from approximately two layers to three layers. Though this event dominates the mean ϵ between 0.1 and 0.9 MPa during the tidal cycle we sampled, much larger values of ϵ were found elsewhere in the inlet. However, these other sites display considerably less stratification; the shear layer may make a significant contribution to the net buoyancy flux in Admiralty Inlet. This may be dynamically more significant than the momentum flux because it directly modifies the density field, which in turn drives the mean baroclinic circulation.

Surprisingly, we find no net energy radiation from the shear layer despite a stratified ambient medium. Indeed, it seems likely there was a net convergence of energy flux into the layer during the hour that we collected measurements. It is questionable how representative this event is of open ocean events. Nevertheless, this study indicates that a local balance of mean and turbulent energy is an adequate description of the turbulent event.

Uncertainties in ϵ and χ_{pe} limit the accuracy of our results. Obviously, more measurements of the dissipation rates while the instability is evolving are needed to more accurately determine P, J_b, $\nabla \cdot \mathbf{J_k}$, and $\nabla \cdot \mathbf{J_p}$. This could be accomplished by using the ADCP to maintain position with respect to the flow at a certain depth, allowing repeated samples in the same water mass. Because the dissipation rates are approximately lognormally distributed, uncertainties in estimates of the mean value decrease slowly, less than $1/(n)^{1/2}$; roughly three times as many profiles would be needed to reduce the uncertainties to 50%. Unfortunately, useful acoustic images are obtained only when moving with respect to the billows. Because the acoustic images are essential to identifying the type of instability, two vessels would be required to significantly improve the accuracy of this energetics analysis.

Lastly, this study outlines a sampling pattern and analysis technique which find reasonable agreement between microstructure measurements and changes in fine-scale density and velocity. In our experience, to find even gross quantitative agreement between microstructure and fine-scale measurements is exceptional. Attempts to find a similar local balance in spatial series from the Strait of Gibraltar using $U/x \rightarrow t$ did not succeed [*Wesson*, 1991]. Advection of horizontal gradients apparently dominates the energy balance. A fluid-following coordinate system, even if it only crudely tracks the flow, simplifies the physics considerably. Model schemes that employ Lagrangian coordinates, like the generalized Lagrangian mean formulation of *Andrews and McIntyre* [1978], would seem the only tractable way to simulate turbulent processes in energetic, highly advective flows such as those in straits and estuaries.

Appendix: Estimating TKE

The shear probes cannot be used to directly measure TKE because their velocities are contaminated by AMP's motions at scales larger than a meter or so. We therefore estimate q by two methods to confirm the validity of the estimators.

From variations in AMP's fall rate we can estimate w' in the billows and hence estimate the turbulent velocity q_w. AMP is a free-falling platform well coupled to the water by small drag screens. Because the profiler has a large vertical drag coefficient, the perturbation in the fall rate should be close to the vertical velocity of the water [*Desaubies and Gregg*, 1978]. For most profiles through the billows, AMP's fall rate is strongly perturbed (Figure A1), varying by ± 5 cm s^{-1} from the typical linear decrease in fall rate. Using 20 AMP profiles to define the average fall rate w_{avg}, we estimate the vertical velocity fluctuation as

$$w'(p) = w_{\text{fall}}(p) - w_{\text{avg}}(p). \qquad \text{(A1)}$$

The rms value of the perturbed fall rate is used as the vertical velocity scale. Because $Re_b \equiv \epsilon/\nu N^2$, where ν is the kinematic viscosity, averages 4×10^4 within the layer during our measurements, we assume isotropy of the dissipation-scale turbulent velocity components [*Gargett et al.*, 1984], $q_w = (3w')^{1/2}$. On the largest

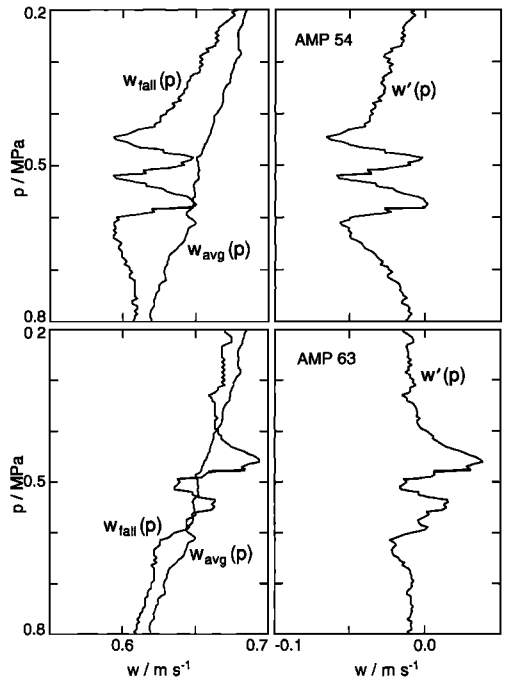

Figure A1. Fall-rate profiles through the billows displaying large perturbations due to the vertical velocity within the billows for (top) AMP 54 and (bottom) AMP 63. Individual and average fall rates are shown in the left panels, their difference is shown in the right panels.

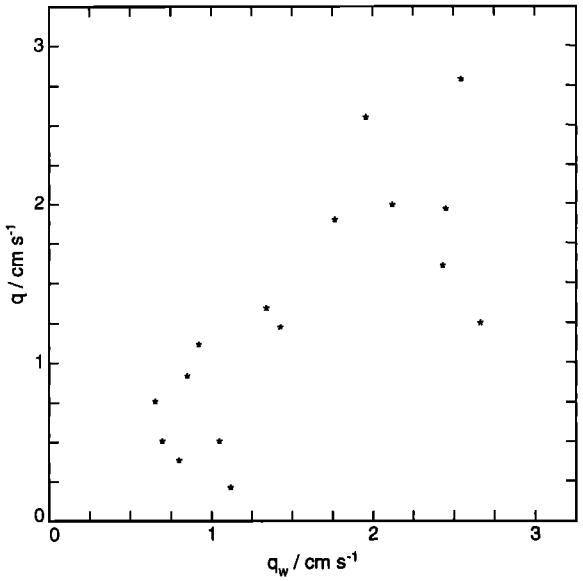

Figure A2. Comparison of turbulent velocity scale q, estimated by the Taylor scaling when $c = 1$, with q_w estimated from fall-rate variations. The linear correlation coefficient and Spearman's ρ equal 0.77. We estimate errors in q as the average difference of the two estimates.

scales of the billows it is obvious the velocity components are not isotropic. Using a ratio of billow height to wavelength of 0.3 to estimate the maximum anisotropy expected, we may underestimate q by a factor of 3.

A classic scaling, developed by *Taylor* [1935], relates q to ϵ and the outer (or integral) scale of the eddies L as $q \equiv (\epsilon L/c)^{1/3}$. A wide variety of constants, $0.04 < c \leq 1$, and length scales have been used owing, in part, to difficulty in defining the largest eddies of the flow with one-dimensional data. On the basis of Taylor's scaling, we estimate q (in meters per second) using

$$q \equiv \Sigma(\frac{1}{c}\epsilon_{ov} L_{max})^{1/3}(L_{max}/d) \qquad \text{(A2)}$$

where L_{max} is the thickness of each overturn (see part 1) within the control volume greater than 2 m, and ϵ_{ov} is the average dissipation rate within each overturn. The factor L_{max}/d weights the TKE associated with each overturn by the fraction of the layer it occupies. Figure A2 compares q and q_w with $c = 1$. Their trends are similar, but $q_w > q$. The two estimates are significantly correlated; both the linear correlation coefficient and Spearman's ρ, a nonparametric correlation coefficient, are 0.77. Averaging over all the drops, $\overline{q} = 1.2$ cm s^{-1} and $\overline{q_w} = 1.6$ cm s^{-1}. Because the two estimates are not wildly different when isotropy is assumed, we conclude that the turbulent velocities are only moderately anisotropic. Use of $c = 0.42$ makes the means equal. On the basis of the average difference between the two estimates, $(1/n)\Sigma(q_w - q) \approx 0.3$, with $c = 1$ and where n is the number of samples, we assume error bounds of $(0.75, 1.33)q$.

Acknowledgments. The collection of these data was funded by Washington State Sea Grant, and the bulk of the analysis was funded by the Office of Naval Research University Research Initiative "Mixing to Mesoscale." H.E.S. was also supported on National Science Foundation grant OCE-9202773. This article benefited greatly from discussions with Kraig Winters, Jim Riley, Eric D'Asaro, David Winkel, and Pete Lombard. This is contribution number 2113 from the School of Oceanography of the University of Washington.

References

Andrews, D. G., and M. E. McIntyre, An exact theory of nonlinear waves on a Lagrangian-mean flow, *J. Fluid Mech., 89*, 609–646, 1978.

Desaubies, Y. J. F., and M. C. Gregg, Observations of internal wave vertical velocities by a free-fall vehicle, *Deep Sea Res., 25*, 933–946, 1978.

Dillon, T. M., and M. M. Park, The available potential energy of overturns as an indicator of mixing in the seasonal thermocline, *J. Geophys. Res., 92*, 5345–5353, 1987.

Fritts, D. C., The excitation of radiating waves and Kelvin-Helmholtz instabilities by the gravity wave-critical level interaction, *J. Atmos. Sci., 36*, 12–23, 1979.

Fritts, D. C., Shear excitation of atmospheric gravity waves, II, Nonlinear radiation from a free shear layer, *J. Atmos. Sci., 41*, 524–537, 1984.

Gargett, A. E., T. R. Osborn, and P. W. Nasmyth, Local isotropy and the decay of turbulence in a stratified fluid, *J. Fluid Mech., 144*, 231–280, 1984.

Geyer, W. R., and J. D. Smith, Shear instability in a highly stratified estuary, *J. Phys. Oceanogr., 17*, 1668–1679, 1987.

Gill, A. E., *Atmosphere-Ocean Dynamics*, 662 pp., Academic, San Diego, Calif., 1982.

Gregg, M. C., Entropy generation in the ocean by small-scale mixing, *J. Phys. Oceanogr., 14*, 688–711, 1984.

Gregg, M. C., Diapycnal mixing in the thermocline: A review, *J. Geophys. Res., 92*, 5249–5286, 1987.

Gregg, M. C., H. Peters, J. C. Wesson, N. S. Oakey, and T. J. Shay, Intensive measurements of turbulence and shear in the equatorial undercurrent, *Nature, 318*, 140–144, 1985.

Ho, C., and P. Huerre, Perturbed free shear layers, *Annu. Rev. Fluid Mech., 16*, 365–424, 1984.

McPhee, M. G., and J. D. Smith, Measurements of the turbulent boundary layer under pack ice, *J. Phys. Oceanogr., 6*, 696–711, 1976.

Monin, A. S., and A. M. Yaglom, *Statistical Fluid Mechanics: Mechanics of Turbulence*, 769 pp., MIT Press, Cambridge, Mass., 1971.

Overland, J. E., Atmospheric boundary layer structure and drag coefficients over sea ice, *J. Geophys. Res., 90*, 9029–9049, 1985.

Price, J. F., M. O. Baringer, R. G. Lueck, G. C. Johnson, I. Ambar, G. Parrilla, A. Cantos, M. A. Kennelly, and T. B. Sanford, Mediterranean outflow mixing and dynamics, *Science, 259*, 1277–1282, 1993.

Seim, H. E., and M. C. Gregg, Detailed observations of a naturally occurring shear instability, *J. Geophys. Res., 99*, 10,049–10,073, 1994.

Taylor, G. I., Statistical theory of turbulence, *Proc. R. Soc. London, A151*, 421–478, 1935.

Tennekes, H., and J. L. Lumley, *A First Course in Turbulence*, 300 pp., MIT Press, Cambridge, Mass., 1972.

Thorpe, S. A., Turbulence in stably stratified fluids: A review of laboratory experiments, *Bound.-Layer Meteor., 5*, 95–119, 1973a.

Thorpe, S. A., Experiments on instability and turbulence in a stratified shear flow. *J. Fluid Mech., 61*, 731–751, 1973b.

Thorpe, S. A., Turbulence and mixing in a Scottish loch, *Phil. Trans. R. Soc. London, A, 286*, 125–181, 1977.

Thorpe, S. A., Transitional phenomena and the development of turbulence in stratified fluids: A review, *J. Geophys. Res., 92*, 5231–5248, 1987.

Wesson, J. C., Turbulence and mixing in the Strait of Gibraltar, Ph.D. dissertation, 317 pp., Univ. of Wash., Seattle, 1991.

Wijesekera, H. W., and T. M. Dillon, Internal waves and mixing in the upper equatorial Pacific Ocean, *J. Geophys. Res., 96*, 7115–7125, 1991.

Wijesekera, H. W., T. M. Dillon, and L. Padman, Some statistical and dynamical properties of turbulence in the oceanic pycnocline, *J. Geophys. Res., 98*, 22,665–22,679, 1993.

Winters, K. B., and E. A. D'Asaro, Three-dimensional instability near a critical level, *J. Fluid Mech., 272*, 255–284, 1994.

Winters, K. B., P. N. Lombard, J. J. Riley, and E. D'Asaro, Available potential energy and mixing in density stratified fluids, *J. Fluid Mech.*, in press, 1995.

M.C. Gregg , Applied Physics Laboratory and School of Oceanography, College of Ocean and Fishery Sciences, University of Washington, 1013 NE 40th Street, Seattle, WA 98105-6698.

H.E. Seim, Clark 3, Woods Hole Oceanographic Institution, Woods Hole, MA 02543.

(Received April 13, 1994; revised October 17, 1994; accepted November 7, 1994.)